



American Society of
Mechanical Engineers

ASME Accepted Manuscript Repository

Institutional Repository Cover Sheet

ASME Paper Title:

Some observations on the computational sensitivity of rotating cavity flows

Authors:

Tom Hickling and Li He

ASME Journal Title:

Journal of Engineering for Gas Turbines and Power

Volume/Issue:

143/4

Date of Publication (VOR* Online):

26 February 2021

ASME Digital Collection URL:

<https://asmedigitalcollection.asme.org/gasturbinespower/article/143/4/041014/1096609/Some-Observations-on-the-Computational-Sensitivity>

DOI:

<https://doi.org/10.1115/1.4049824>

*VOR (version of record)

Some Observations on the Computational Sensitivity of Rotating Cavity Flows

Tom Hickling*

Department of Engineering Science

University of Oxford

Oxford OX1 3PJ, UK

tom.hickling@eng.ox.ac.uk

Li He

Department of Engineering Science

University of Oxford

Oxford OX1 3PJ, UK

li.he@eng.ox.ac.uk

ABSTRACT

Across the open literature, there is no clear consensus on what the most suitable modelling fidelity is for rotating cavity flows. Although it is a widely held opinion that URANS approaches are unsuitable, many authors have succeeded in getting reasonable heat transfer results with them. There is also a lack of research into the validity of hybrid URANS/LES type approaches such as DES. This paper addresses these research challenges with a systematic investigation of a rotating cavity with axial throughflow at Grashof numbers of 3.03×10^9 and 3.03×10^{11} .

The disk near-wall layers remained laminar at both conditions, meaning that a turbulence model should not be active in these regions. The disk heat transfer was observed to affect the near-disk aerodynamics, which in turn affect the disk heat transfer: this feedback loop implies that conjugate heat transfer computations of rotating cavities may be worth investigating. On the shroud, additional eddy viscosity in URANS and DES was found to interfere with the formation of heat transfer enhancing streaks, whilst these were always captured by LES.

DES exhibited a concerning behaviour at the higher Grashof number. Locally generated eddy viscosity from the shroud was injected into the bulk fluid by the radial inflow. This contaminated the entire cavity with non-physical

*Address all correspondence to this author.

modelled turbulence. As the radial inflow is a characteristic feature of rotating cavity flows, these results show that caution is necessary when applying hybrid URANS/LES approaches to this type of flow.

1 Introduction

1.1 Background

As new engine architectures such as open rotor and embedded distributed engines come to the fore, it has become apparent that core sizes are likely to shrink. As smaller core sizes generally lead to increased tip clearance losses (particularly in HP compressors) [1] there is a need to understand the flow and heat transfer in compressor internal air system cavities so that the radial growth of the compressor disks (and hence change in tip clearance) can be predicted.

The shroud (shown in Fig. 1) is often hotter than the disk cobs, which are cooled by axial throughflow; this establishes an unstable temperature gradient in the cavity [2]. The unstable temperature gradient interacts with the centrifugal and Coriolis pseudo-forces to form a large-scale inertial wave-like flow structure that consists of pairs of circulations that slip relative to the cavity at a speed of about 10% of the cavities rotational speed [3]. A diagram of this flow structure, containing one circulation pair, is shown in Fig. 2.

The reason for the formation of these flow structures is quite well established, and can be derived from the inviscid linear equations for a rotating fluid. Cyclonic circulations have a reduced pressure, and anticyclonic circulations have an elevated pressure. These pressure differences are illustrated in Fig. 2 by the $+\Delta p$ and $-\Delta p$ symbols respectively. A pair of cyclonic and anticyclonic circulations create alternating regions of low and high pressure, generating the circumferential pressure gradient necessary for radial flow [3]. The strength of the radial flow is dependent on the strength of the circulations, which affects the strength of the circumferential pressure gradients. This in turn influences the strength of the radial flow. Through this feedback loop the possibility for self-excited disturbances to develop into sustained large scale patterns can be seen [4]. Three dimensionless parameters are necessary to describe the operating conditions of a rotating cavity with axial throughflow. These are the axial Reynolds number Re_z , the rotational Reynolds number Re_ϕ , and the buoyancy parameter $\beta\Delta T$. These are given by

$$Re_z = \frac{V_z D}{\nu_{in}} \quad (1)$$

$$Re_\phi = \frac{\Omega b^2}{\nu_{in}} \quad (2)$$

$$\beta\Delta T_{max} = \frac{T_{max} - T_{in}}{T_{in}} \quad (3)$$

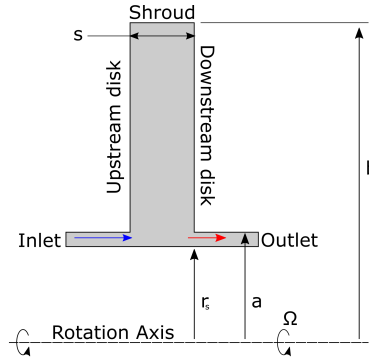


Fig. 1. General cavity diagram and nomenclature.

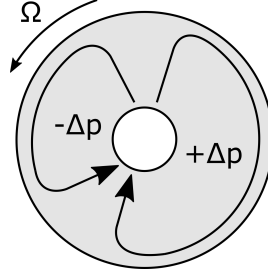


Fig. 2. Typical rotating cavity flow structure.

where the bore hydraulic diameter, D is given by $D = 2(a - r_s)$, Ω is the rotational speed of the cavity, and V_z is the velocity of the axial throughflow. T_{\max} and T_{in} are the maximum disk temperature and the inlet temperature of the throughflow, and a , b , and r_s are geometric parameters defined in Fig. 1. Engine representative orders of magnitude for Re_z , Re_ϕ , and $\beta\Delta T$ are 10^5 , 10^6 , and 10^{-1} , respectively [3].

The definition for the Grashof number used in this report is given by

$$\text{Gr} = \left(1 - \frac{a}{b}\right)^3 \text{Re}_\phi^2 \beta \Delta T_{\max}. \quad (4)$$

The Rayleigh number can be calculated by multiplying Gr by the Prandtl number. An engine representative value for the Rayleigh number is 10^{12} [3]. The disk Nusselt number is defined as

$$\text{Nu}_d = \frac{qr}{k\Delta T_w}, \quad (5)$$

where q is the local heat flux, k is the fluid thermal conductivity, and ΔT_w is the local temperature difference between the axial throughflow and the disk. It is important to note that this is not a true Nusselt number in that it does not represent the ratio of convective to conductive heat transfer, it is just a conveniently normalised heat flux. The shroud Nusselt number Nu_{sh} is defined in the same way, except half the cavity width ($s/2$) is used as the length scale in place of r .

1.2 Experimental Investigations

A thorough review of all work carried out on rotating cavities pre-2015 was published by Owen and Long [3]. Three experimental rigs that have provided data sets used for the validation of numerical studies on open rotating cavities with axial throughflow are briefly noted here: the measurements of Farthing et al. [5], Long [6], and Long and Tucker [7] on the University of Sussex single cavity rig; the measurements of Bohn et al. [8] on the RWTH Aachen University single cavity rig; and the measurements of several authors (e.g. Atkins and Kanjirakkad [9], Puttock Brown et al. [10]) on various builds of the Multiple Cavity Rig facility at the University of Sussex. In this paper, the focus is on rotating cavities with axial throughflow, although there have been several investigations on cavities with radial in/outflow [1, 11], and closed cavities [12].

1.3 Computational Investigations

There is a clear hierarchy in terms of modelling fidelity for unsteady flows [13] from bottom to top: URANS, URANS/LES hybrids, LES, and finally DNS. Previous simulations with URANS, hybrids, and LES are discussed below.

Coarse mesh NLES: Many computational fluid dynamics (CFD) analyses of rotating cavities with axial throughflow have used laminar computations with large cell sizes. This is effectively a numerical LES (NLES) that is able to resolve only the very largest eddies and implicitly models the sub-grid effects with numerical dissipation from the discretization scheme. In some flows, this kind of simulation performs better than URANS [14].

These computations often captured an unsteady number of circulations; Long and Tucker [15] found that the flow vacillated between one and two radial arms, and Bohn et al. [16–18] captured a limit cycle behaviour where the flow oscillated between one, two, and three circulation pairs. The durations of these oscillations were found to correspond to experimental smoke flow visualisation.

To reduce the computational cost of these simulations He [4] modelled the same case as [16] using a Fourier spectral decomposition in the tangential direction to capture the large scale circulations. Six or seven harmonics were found to be sufficient to accurately reproduce the shroud heat flux from a 300 circumferential cell base mesh, this corresponded to a 20- to 23-fold reduction in the number of cells to be solved. Both the base and Fourier harmonic solution failed to reproduce the pattern transition found in [16]. However, the number of circulation pairs was found to be sensitive to inlet total pressure distortions.

URANS: It has been suggested that URANS is not suitable for turbulence modelling in rotating cavities; Tucker [19] claimed that compressor cavity flows had ‘proved hopeless for URANS type modelling’. This lack of trust in URANS can be attributed to the need for a spectral gap between the resolved coherent scales and modelled stochastic unsteadiness [20], and double counting of unsteady turbulent structures in regimes such as wake flows and vortex shedding [14, 21].

A further issue is the advection of locally generated eddy viscosity to regions where it is unphysical. This effect has been noted in a HP turbine cascade by Yao and He [14], where eddy viscosity generated upstream was advected to the trailing edge where it interfered with unsteady vortex shedding.

Even when the above considerations are not an issue, URANS is limited by its inherent empirical nature; it is well

known to struggle to capture the effects of buoyancy, stratification, rotation, streamline curvature, and transition. The latter is aggravated by a wall heat flux, which contributes to destabilising laminar boundary layers [22]. All of these are relevant for rotating cavity flows. It is therefore confusing that many simulations that have been conducted with URANS [10, 23–26] have provided reasonable predictions of the disk heat flux.

URANS has a consistent issue with accurately predicting the shroud heat transfer, particularly at higher rotational speeds, as seen in computations by Sun et al. [27] and Puttock-Brown et al. [28] (with the latter under-predicting the heat flux by 31%). Having said that, URANS has been used to investigate near-shroud flow structures with some success - Puttock-Brown et al. [10, 28] carried out high resolution URANS computations at Grashof numbers of between 7.94×10^{11} and 8.94×10^{11} . These simulations predicted the presence of streaks, a previously unobserved flow structure. The streaks took the form of counter rotating vortices in the near shroud region of cyclonic circulations, and were proposed to be formed by buoyancy effects. The streaks modified the local Nusselt number by as much as 40%, but have yet to be seen experimentally. To the authors' knowledge, these streaks have never been captured using LES, even though one would expect them to be present when the turbulence model intends to resolve the smaller scales of the flow. Thus, if streaks are a universal feature of rotating cavity flows, it is of interest to know whether URANS can consistently model them, or if higher fidelity methods are necessary for a confident prediction of shroud heat transfer.

URANS/LES hybrids: Hybrid URANS/LES computations have been used several times to model rotating cavity flows. Atkins and Kanjirakkad [9] carried out two hybrid URANS/NLES computations at Grashof numbers of up to 7.73×10^{11} . At higher rotational speeds, the shroud heat flux reversed the local density gradient, generating buoyant structures that reduce the temperature at higher radii. This effect was also observed in experimental data in the same paper.

Tateishi et al. [29] carried out a detached eddy simulation (DES) of a full compressor internal flow path. The authors observed interaction effects between the cavities, in particular the formation of a hot cell by radial inflow.

Very Large Eddy Simulations using a Lattice-Boltzmann solver were reported by Kouwa et al. [30] at Grashof numbers of up to 7.17×10^{11} . The mesh was refined locally around walls and in the axial throughflow-cavity shear layer. The results were verified with a mesh refinement study and validated with experimental disk heat transfer data.

Focus has generally been on the ability of URANS/LES hybrid methods to eliminate the excessive computational cost of resolving the near-wall region with LES. There has been little consideration of the validity of these methods for heat transfer in rotating cavities - their performance is expected to be limited by the performance of the URANS model in the near-wall layer, which is critical for heat transfer. The near-wall region is high gradient and thus highly sensitive. Any uncertainty created by the near-wall switch of modelling fidelity may have a significant effect on the wall heat transfer [31]. Even in isothermal flows, there is uncertainty due to the well-known issues of grid-induced separation, modelled stress depletion, and the "grey area" where the simulation is neither URANS nor LES.

LES: LES is the highest fidelity method considered in this report, and the least empirical. The first reported LES computations on rotating cavities were by Sun et al. in 2007 [27]. LES was found to give a much higher shroud heat flux than URANS, and had errors (compared to experimental data) that were in the range of -25% to 6% . The -25% error in the

shroud heat flux was at $Gr = 1.01 \times 10^{11}$, the highest Grashof number simulated.

Tan et al. [24] compared URANS and LES computations on the experimental data of Bohn [8] at a Grashof number of 3.03×10^9 . They found URANS and LES gave similar errors in the prediction of disk heat transfer, although the LES disk heat flux fluctuated significantly more than that of URANS.

LES computations at a Grashof number of 1.88×10^8 were reported by Pitz et al. [32]. Of particular interest in these computations was that the computed kinetic boundary layer thickness (based on the peak magnitude of the radial velocity fluctuations) was found to closely match the theoretical laminar Ekman layer thickness. In a closed rotating cavity, Pitz et al. [33] used the same method for determining the Ekman layer to show that the scaling of the disk boundary layer thickness remained consistent with a laminar Ekman layer at a similar Grashof number.

A recent development has been the LES of compressor cavities with radial inflow [34–36]. The attraction of radial inflow is that it has been found to reduce the disk thermal response time, thus allowing for smaller cold tip clearances [1]. These papers have focussed on regimes where the radial inflow is assumed to suppress the large scale circulations, so that truncated domains can be used. In [35], the transition of the Ekman layer from laminar to turbulent was captured. The Ekman layer formed instabilities, and eventually became turbulent at inner radii. The heat transfer in one of these cavities was investigated in [36]. LES was found to give considerably better results than both the URANS models tested. This was due to the excessive viscosity from the URANS solutions affecting the flow structure where the radial inflow is admitted at the shroud, preventing buoyancy effects from occurring. The need to test URANS/LES hybrids was also identified.

Meshing for LES: The usual approach to assessing the wall resolution of simulations is to look at the value of the normalised wall distance - Tan et al. [24] and Sun et al. [27] provide examples of this for LES. The general wall resolution requirement for LES of channel flow is normal, stream-wise, and span-wise spacings of less than 1, 50, and 15 units, respectively [37]. Whether this is valid for rotating cavity flows is unclear - neither the disk or the shroud near-wall layers are similar to the classical boundary layers on which these requirements are based.

The mesh sizes and Grashof number of some previous simulations of rotating cavities are plotted in Fig. 3. There is no clear separation between the mesh sizes for the different modelling fidelities - one would expect three clear groupings, one for each of LES, URANS/LES hybrids, and URANS (from large mesh counts to small). Here, we see that some URANS and LES meshes are often of a similar size, and that, unexpectedly, hybrid computations have used larger mesh sizes than the LES computations that claim to resolve the near-wall flow at similar conditions.

There is a degree of inconsistency in how modelling and meshing for rotating cavity flows is approached. This paper aims to contribute to a clearer understanding of the behaviour and relevant scales of the flow to enable CFD practitioners to make more informed choices on what modelling fidelities and mesh resolutions are appropriate to use, and where.

1.4 Issues of Interest

The aim of this paper is to shed some light on the simulation of rotating cavity flows by addressing the following questions:

1. What are the relevant flow mechanisms and structures in rotating cavity flows?

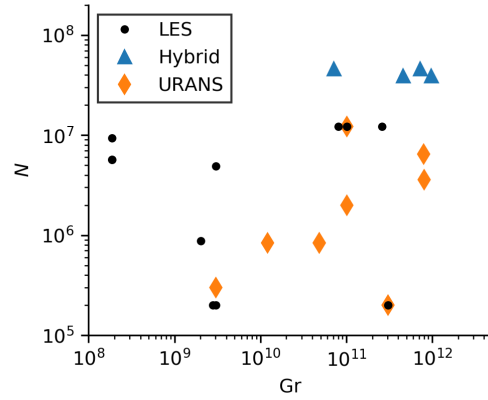


Fig. 3. Mesh scaling of previous simulations of rotating cavities.

2. How do these structures respond to different modelling fidelities and mesh resolutions?
3. Is it necessary to include the interaction of the cavity flow and disk material to realistically simulate the cavity aerodynamics?

In the remainder of this paper, the investigational approach, test case, and then computational methodology are detailed before the results of a validation and verification study are presented. Then, the disk and shroud heat transfer at the low Grashof number condition are discussed in view of the above research questions, before the results of DES and LES at the high Grashof number condition are examined.

2 Methodology

2.1 Investigational Approach

The broad approach of this study is to simulate a rotating cavity at different modelling fidelities, mesh sizes, and thermal boundary conditions. The solver and numerics are kept the same so that any differences between simulations are due to modelling fidelity or thermal boundary conditions alone.

The models used were the $k - \omega$ SST model [38] for URANS, the WALE sub-grid scale (SGS) model [39] for LES, and the Shielded-DES [40] for the URANS/LES hybrid model.

2.2 Test Case

The experimental rig of Bohn et al. [8] at RWTH Aachen is used as the test case in this work. The cavity has co-rotating disks, shroud, and shaft. In [8], the disk temperature profile was created using electrical heaters embedded in aluminium rings so that they supplied an isothermal heat flux to the cavity. The disk heat flux was measured using thermistors placed on both sides of 5 mm plastic disks positioned between the heaters and the cavity. The flow was observed to be laminar (although additional small vortices are superposed onto the large-scale flow structure), and consisted of a single circulation pair, as illustrated in Fig. 2. The flow structure was observed to rotate at 88-90% of the cavity rotational speed.

This rig is a popular validation case for rotating cavity simulations, having been used for both URANS [24, 25, 41] and

Table 1. Experimental conditions and geometry of Bohn et al. [8].

Parameter	Value	Parameter	Value
Re_z	3×10^3	r_{in}	0.12 m
Re_ϕ	2×10^5	a	0.138 m
$\beta\Delta T_{max}$	0.27	b	0.4 m
Ro	0.483	s	0.08 m
Gr	3.03×10^9	Ω	135.28 rpm

LES [24] computations. The experimental conditions used are given in Tab. 1. Note that in [8], an alternative definition for Re_z of $Re'_z = V_z 2a / \nu_{in} = 2 \times 10^4$ is used. The definition used in this paper was chosen to be more consistent with recent research.

2.3 Computational Methodology

The simulations were conducted in the non-inertial frame using the fully compressible pressure-based segregated approach in ANSYS Fluent. This solver is a popular choice for internal flows and heat transfer. To match experimental conditions as closely as possible, a gravity vector that was fixed in the inertial frame (i.e. rotating at $-\Omega$ in the non-inertial frame) was also included. In the computations of Bohn et al. [16] this was found to be essential to create the initial instability that developed into the large scale flow structure.

To avoid confusion of the effects of modelling fidelity/boundary conditions and numerics, the same numerics were used for all simulations. Pressure and velocity were coupled using the SIMPLEC scheme, and unless stated otherwise, the second order upwind scheme was used.

Time was discretized implicitly using a second-order accurate backwards difference, and convergence at each time-step was judged to be when the residuals had dropped by two orders of magnitude. For LES and DES, time steps were set to give CFL numbers of less than one in the bore. CFL numbers were generally much lower inside the cavity. For the 6M cell mesh, this resulted in 700 time-steps per revolution. URANS solutions used time steps that were four times larger than the LES solutions on the same mesh.

Simulations were initialised from a steady RANS solution and were run for 20 revolutions until initial transients had disappeared. This was monitored by tracking the disk and shroud heat fluxes. The simulations were then run for another 20 revolutions to capture flow statistics.

Four different meshes were used, with nominal sizes of 1M, 2M, 4M, and 6M cells. The meshes were fully hexahedral and created by meshing the meridional plane in 2D and then rotating the resulting mesh around the z -axis. The 1M cell mesh is shown in Fig. 4. URANS computations were carried out on the 1M, 2M, and 4M cell meshes, while DES and LES computations used the 2M, 4M, and 6M cell meshes.

For the boundary conditions, total pressure inlets and static pressure outlets were used to match Re_z , and the air inlet temperature was set to 298.15 K. The disk wall temperatures were set to match the distributions given by Bohn et al. [8]

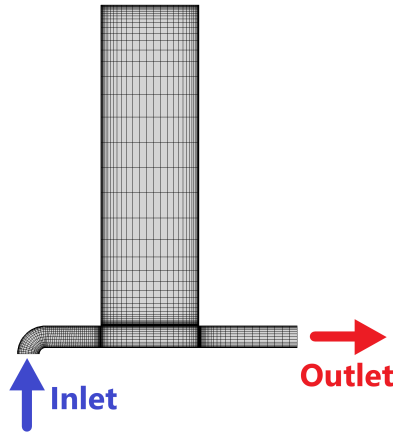


Fig. 4. Meridional view of 1m cell mesh.

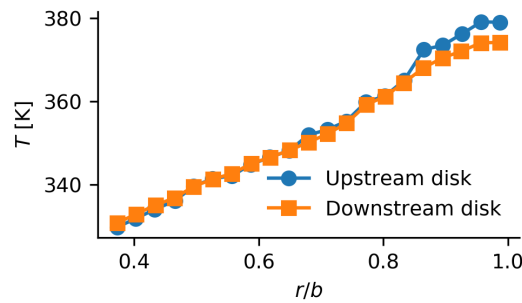


Fig. 5. Experimental disk temperature profiles from [8].

(Fig. 5). The shroud temperature was set to be 353.15 K, in accordance with data in [17] - no value for the shroud temperature was given in [8] which had an unheated shroud. An adiabatic shroud was not used because the unheated shroud still provides a heat flux to the fluid (due to conduction in the test rig), and the formation of streaks (a flow structure of interest in this paper) is caused by the shroud heat flux [28]. Air was modelled as a perfect gas, and temperature dependent values for dynamic viscosity and thermal conductivity were used.

3 Validation and Verification

3.1 Large Scale Flow Structure

The large scale flow structure from the LES simulation on the 6M cell mesh is visible in the temperature contours in Fig. 6. It consists of two circulation pairs (marked with arrows) that rotate at approximately 0.925Ω in the inertial frame. The cyclonic circulations are marked with ‘ $-\Delta p$ ’, and the anti-cyclonic circulations with ‘ $+\Delta p$ ’. The location of the radial arms can clearly be seen by the presence of cold fluid. This flow structure is in agreement with the computations of other authors (e.g. Tan et al. [24]) on this case, although Bohn et al. only observed one circulation pair that slips at $0.88 - 0.90\Omega$ in an experimental smoke flow visualisation [8].

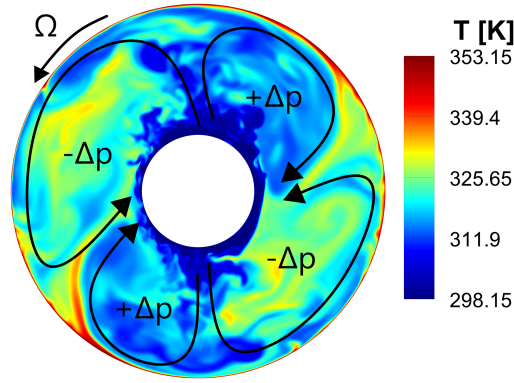


Fig. 6. Mid-plane temperature distribution and large scale flow structure.

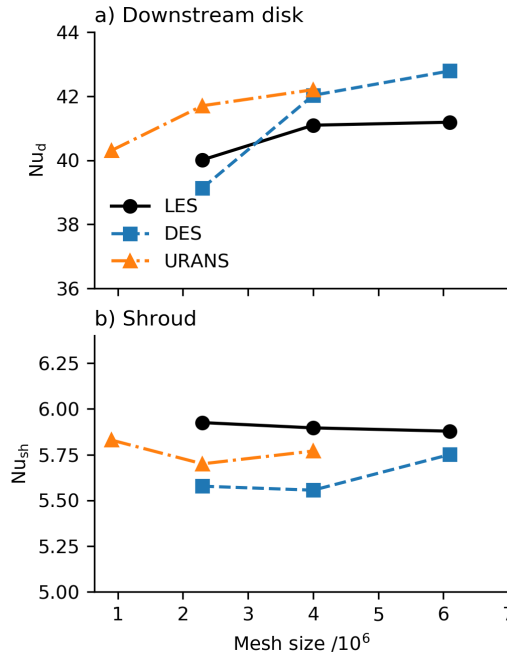


Fig. 7. Average Nusselt number mesh dependencies.

3.2 Mesh Resolution

The mesh dependencies of the average downstream Nu_d and average Nu_{sh} are shown in Fig. 7 for URANS, DES, and LES. On the disk, all three modelling fidelities are converging to mesh independent values, as expected. The picture on the shroud is less clear - there is no convergence of Nu_{sh} , although the size of the mesh dependency is small. It may be that a finer mesh is needed in this area; this is investigated later on in the paper.

To further verify the turbulence resolving simulations, the power spectra of the Turbulent Kinetic Energy (TKE) was calculated at the mid-radial, mid-axial position ($r/b = 0.6725, z/s = 0$) in the cavity. The Power Spectral Density (PSD) of the TKE was calculated as

$$\text{PSD}(\text{TKE}) = [\text{PSD}(u') + \text{PSD}(v') + \text{PSD}(w')] / 2, \quad (6)$$

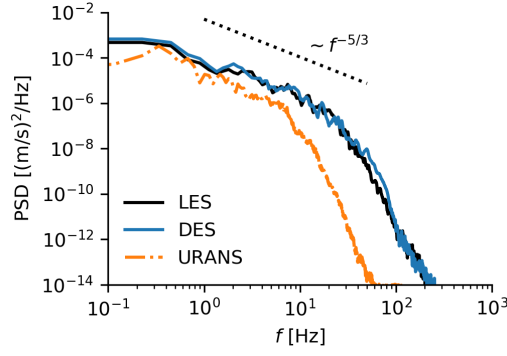


Fig. 8. TKE power spectra at mid-cavity.

where the PSD of each velocity component was calculating using Welch's method (using a Hann window, three segments, and 50% overlap) to reduce finite sampling effects. The results are shown in Fig. 8: a $-5/3$ inertial range is present in each spectra until approximately 25 Hz, indicating that the dynamics of the turbulent flow are appropriately resolved. This is even the case for URANS up until 6 Hz, indicating that it is resolving some stochastic fluctuations that should already be accounted for by the RANS model. LES and DES behave equally well in the bulk flow, as expected. Interestingly, at low frequencies, URANS is not far away from LES. Similar results were observed for the 4M and 2M cell simulations, with the 4M cell mesh giving an identical spectra to the 6M cell mesh with LES.

The wall spacings used are suitable for wall-resolved LES by the classical boundary layer requirements [37] - the average axial, radial, and tangential mesh spacings on the 6M cell mesh are $\Delta r^+ = 21$, $\Delta(r\phi)^+ = 27$, and $z^+ = 0.28$ on the downstream disk, and $r^+ = 0.22$, $\Delta(r\phi)^+ = 25$, and $\Delta z^+ = 5.2$ on the shroud.

3.3 Comparison to Experimental Data

Figure 9 shows a comparison of the computational and experimental time-and-circumferential average Nu_d on the upstream and downstream disks of the cavity. The temperatures used to calculate Nu_d are shown in Fig. 5. The computations reported are on the largest mesh used for each modelling fidelity (4M mesh for URANS, and the 6M cell mesh for DES and LES). The agreement with the experimental data is reasonable; on the upstream disk there is a close correspondence between the experimental and computational heat transfer for all modelling fidelities. On the downstream disk, the agreement is less good. At very low radii ($r/b < 0.5$) there is a significant over-prediction in Nu_d present in all simulations - this phenomena was observed to be completely mesh independent and due to the impingement of the cold axial throughflow upon the heated disk. This is a feature of most other computations on this test case [24, 25, 41], although in [41] the magnitude of the over-prediction was found to reduce with the inclusion of conjugate heat transfer (CHT). At higher radii on the downstream disk the heat flux is still over-predicted.

4 Near-Disk Flow

The computed disk heat transfer has little dependence on the modelling fidelity (demonstrated in Figs. 7 and 9). This is because of the nature of the laminar nature of the disk near-wall layers - no structures consistent with Ekman layer transition

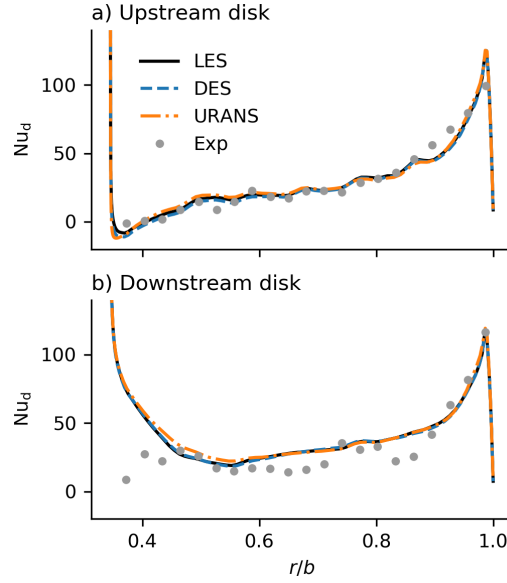


Fig. 9. Disk Nusselt number distributions. Experimental data from [8].

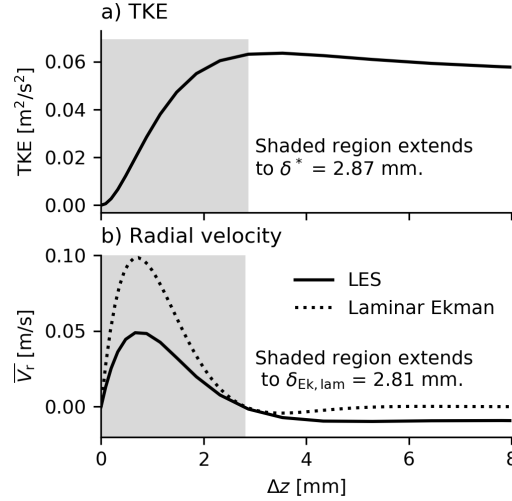


Fig. 10. Upstream disk near-wall layer behaviour at mid-radius.

(for an example of these in a cavity with radial inflow, see [35]) were observed in the LES solutions. Although near-disk unsteadiness was observed in our computations, this was driven by external unsteadiness and was parallel to the disk, and not generated by local near-wall layer instabilities that create heat transfer enhancing wall-normal transport of fluid.

The TKE at the mid-radial location is plotted against the distance from the upstream disk (Δz) in Fig. 10a. The lack of strong peak is evidence for the laminar nature of the near-disk layer: in a turbulent boundary layer, a peak in the TKE distribution due to turbulent production is expected within the buffer layer ($5 < y^+ < 30$). The peak location of TKE occurs at $\Delta z = 2.87 \text{ mm}$, or $z^+ = 18.0$. The very shallow TKE peak in Fig. 10a thus implies that, within the near-disk layer, the production of TKE is very low, whereas its dissipation by viscous effects is still clearly appreciable, as shown by the TKE dropping to zero at the wall. This behaviour is consistent with a laminar Ekman layer driven by external unsteadiness.

The theoretical linear laminar Ekman layer thickness can be estimated as

$$\delta_{\text{Ek,lam}} = \pi b / \text{Re}_\phi^{0.5} = 2.81 \text{ mm}, \quad (7)$$

this is the location of the first zero crossing point of a laminar Ekman layer, whose velocity is given by

$$V_r = -V_{\phi,\text{core}} e^{-\pi \Delta z / \delta_{\text{Ek}}} \sin\left(\frac{\pi \Delta z}{\delta_{\text{Ek}}}\right), \quad (8)$$

where $V_{\phi,\text{core}}$ is the relative tangential velocity of the fluid away from the disks [42]. The radial velocity profile is plotted in Fig. 10b. Despite the different magnitudes of the peak radial velocity, the computational near-wall layer behaves in a similar way to the theoretical laminar Ekman layer - the peaks are in the same location, and the zero-crossing points are almost identical.

By assuming a Blasius 1/7 power law profile [42], the turbulent Ekman layer thickness can also be estimated as

$$\delta_{\text{Ek,turb}} = 0.0983 b \text{Re}_\phi^{-0.5} \left(\frac{|V_{\phi,\text{core}}|}{\Omega b} \right)^{0.6} = 0.58 \text{ mm}. \quad (9)$$

Taking a similar approach as Pitz et al. [32, 33], and using the location of peak TKE, δ^* , as the upper limit of the disk near-wall layer, we find that the near-wall layer thickness is more consistent with the thickness predicted by laminar Ekman layer theory and over four times thicker than the turbulent theory. These results are tabulated for the upstream disk of the cavity at the mid-radial position in Tab. 2.

Table 2. Computed upstream disk near-wall layer thickness at the mid-radial location.

Case	LES	DES	URANS
δ^* [mm]	2.87	2.87	3.22

These results explain the reasonable predictions in the literature with URANS - as the disk near-wall layers are laminar, there are no potentially heat transfer enhancing vortical structures to resolve or model within them. Thus, as long as the behaviour of the off-wall flow is captured accurately, URANS or URANS/LES hybrid approaches should be suitable when the Grashof number is low enough to avoid transition or the presence of significant modelled turbulence within the disk Ekman layer.

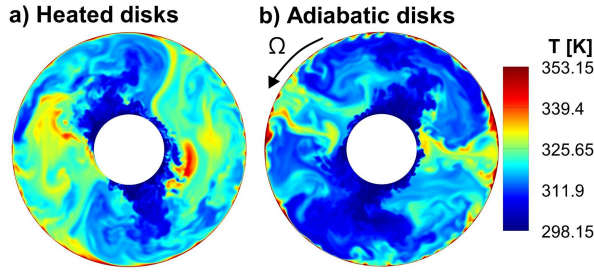


Fig. 11. Mid-plane temperatures with isothermal and adiabatic disks.

5 Disk Thermal Boundary Condition

5.1 Thermal Boundary Condition Background

In the literature, there has been little consideration on what thermal boundary condition is suitable to properly capture the dynamics of rotating cavity flows. Most simulations use isothermal boundary conditions (i.e. the temperature on each boundary face does not change throughout the computation) to match time-mean experimental data. To the authors' knowledge the only simulation where the feedback between the fluid and solid domain has been captured was by Tian et al. [41], who found a significant reduction in disk Nusselt number at low radii but did not report any changes in the cavity flow structure.

To assess whether it is necessary to include conjugate effects, extra LES simulations were conducted on the 2M and 6M cell mesh.

These simulations were conducted using two types of boundary conditions - the first case uses heated isothermal disks as in the previous simulations in this paper. In the second case, the disks were both set to be adiabatic, and the shroud temperature was adjusted so that the difference between the maximum disk temperature and the throughflow was the same as in the baseline heated disk case. In contrast to the rest of this paper, the simulations in this section used a bounded central differencing discretization for all variables.

5.2 Effects on Flow Structure

The global flow structure with adiabatic disks is unchanged from the isothermal disk case, with two circulation pairs forming in both simulations although the temperature and relative extent of the cyclonic and anti-cyclonic circulations has changed (see Fig. 11). Despite the similarity in the large-scale flows structure between the two cases, the disk thermal boundary condition has a significant effect on the evolution of the disk temperatures and the aerodynamic characteristics of the near-wall flow.

The mean temperature distributions that develop on the adiabatic and isothermal downstream disks are shown in Fig. 12. The temperature distribution that develops on the adiabatic disks is very different to the temperature imposed on its isothermal counterpart to match the data of Bohn et al. [8].

Figure 13 shows the mean radial shear stress for both disk boundary conditions for simulations conducted on the 6M cell mesh. When an isothermal boundary condition is used for the disks, the buoyancy forces from the positive radial temperature gradient in the near-wall fluid drives a near-wall radial inflow above $r/b \approx 0.8$. In contrast, for the adiabatic disks, the near-wall temperature gradient is governed by aerodynamic interactions between the flow in the cavity and the disk, and any

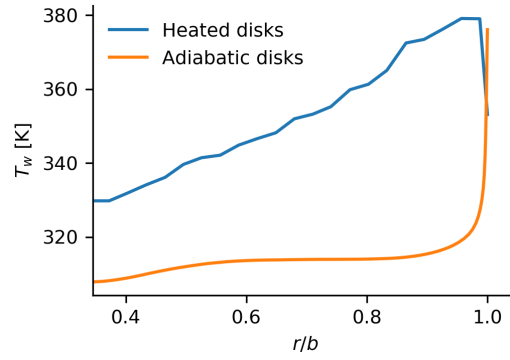


Fig. 12. Fluid wall temperature on the downstream disk.

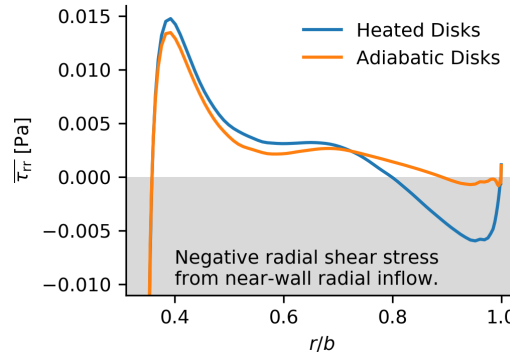


Fig. 13. Average radial shear stresses on downstream disk.

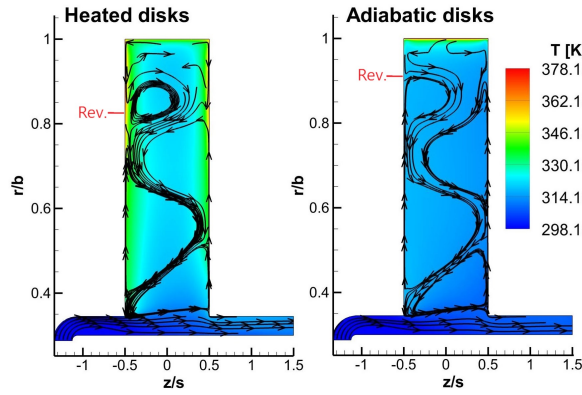


Fig. 14. Time-average temperature and meridional velocity streamlines.

near-wall radial inflow occurs at a higher radius ($r/b > 0.9$) and is of a much smaller velocity. This phenomena is mesh independent, with very close agreement in the values of the shear stress on the 2M and 6M cell meshes.

The meridional velocity streamlines in Fig. 14 also show this effect. The location of the reversal in near-disk flow is marked with 'Rev.'; this occurs at locations corresponding to the reversal of the radial disk shear-stress in Fig. 13.

This difference in behaviour of the near wall is caused by the local buoyancy forces generated by the wall: when the wall is isothermal, the wall radial temperature gradient generates a radially inward buoyancy force. When the disks are adiabatic, most of the disk has a very small radial temperature gradient (see Fig. 12), meaning that there is a comparatively small buoyancy force, and that the behaviour of the near-wall flow is governed only by the flow structures in the flow away

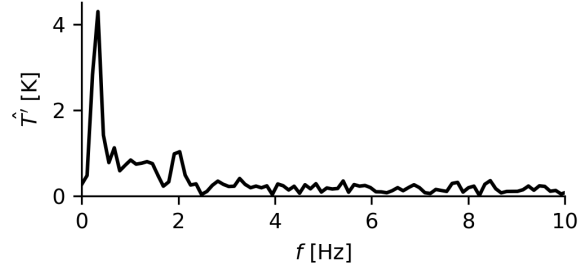


Fig. 15. Temperature spectrum adjacent to the downstream disk.

from the disk.

5.3 Conjugate Heat Transfer and Rotating Cavities

If the aerodynamics within the cavity influenced the disk heat transfer in a one-way coupling (i.e. the disk shear stress was independent of the thermal boundary condition), isothermal simulations would - with correct boundary conditions - be sufficient to capture the cavity aerodynamics. However, the results in this section are indicative of a two-way relationship, where the aerodynamics influence the disk heat transfer, which also feeds back into the aerodynamics. As there is this two-way relationship, it is likely that it will be necessary to capture the interaction of the fluid and solid domain in a conjugate heat transfer computation to properly reproduce the cavity aerodynamics.

It is interesting to consider now whether it is possible to accurately capture the flow aerodynamics by simulating a steady solid domain or whether a fully unsteady approach is necessary. Figure 15 shows the temperature spectra at a point on the mid-radial position 1.25 mm from the downstream disk from the isothermal simulation. The dominant harmonic (amplitude 4 K) in this spectrum is at a very low frequency; its location at $f = 0.34$ Hz implies that the slip ratio of the flow structure relative to the cavity is

$$\frac{\Omega_{\text{core}}}{\Omega} = 1 - \frac{1}{N_{\text{arms}}} \left(\frac{2\pi f}{\Omega} \right)_{\text{peak}} = 0.925 \quad (10)$$

where N_{arms} , the number of radial arms, is two. When calculating the slip ratio directly from the average tangential velocity in the simulation, one finds that $\Omega_{\text{core}}/\Omega = 0.923$ - the dominant harmonic is due to the slip of the large-scale flow structure.

Comparing representative spatial scales of the near-interface temperature fluctuations in both the fluid and solid domains is useful to examine whether the low frequency temperature fluctuations will have an effect on the solid domain [43]. On the fluid side, the representative scale is the size of the near-wall eddies, roughly equivalent to the near-wall layer thickness, which for these simulations was $\delta^* = 2.87$ mm. (Fig. 10.) On the solid side, the representative scale is the thermal penetration depth, which is calculated following Faghri et al. [44]. The penetration depth of a temperature fluctuation with time-scale

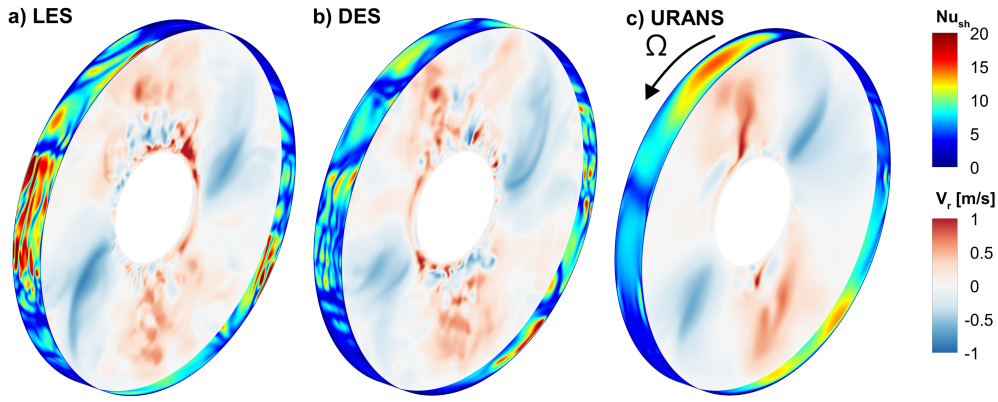


Fig. 16. Contours of shroud Nusselt number and mid-plane radial velocities at the low Grashof number condition.

$1/f$ can be calculated from

$$\delta_p = \sqrt{8\alpha/f} = 22.9 \text{ mm}, \quad (11)$$

where $\alpha = k/\rho c$ and the properties of Nickel Steel are used for the disks ($k = 80 \text{ W/mK}$, $\rho = 8000 \text{ kg/m}^3$, and $c = 450 \text{ J/kgK}$). The representative solid spatial scale is significantly larger than the corresponding fluid scale, and also implies that that fluid temperature fluctuations will penetrate a significant distance into the solid domain and feedback in to the fluid. As the unsteady response of the solid domain would have a dominant influence on the fluid domain wall temperature, there is an interaction between the two domains here that implies that including unsteady CHT effects may have an effect on predicting heat transfer rotating cavities and is certainly worth investigating.

6 Near-Shroud Flow

6.1 Shroud Streaks

Although shroud streaks have been observed at engine relevant Grashof numbers in URANS simulations [10, 28], to the authors' knowledge they have not previously featured in papers that use higher fidelity methods such as LES at any Grashof number. Both LES and DES capture streaks - their existence can be seen in the Nu_{sh} contours in Fig. 16 (along with the radial velocity on the cavity mid-plane), where they occur in cyclonic circulations, in accordance with the observations of Puttock-Brown et al. [10, 28]. Despite streaks only being captured in the present LES and DES (Fig. 16a, b), all three simulation methods give similar values for Nu_{sh} , with LES giving a heat flux that is approximately 2% higher than both DES and URANS (Fig. 7b). Investigating what mesh resolutions and modelling fidelities are appropriate for capturing these streaks is the focus of the rest of this section.

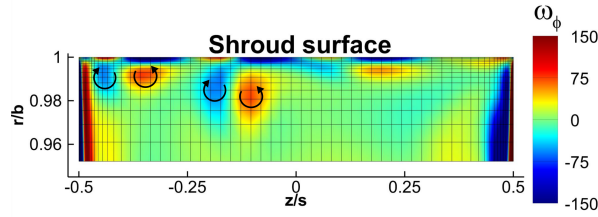


Fig. 17. Streak tangential vorticity at the low grashof number condition. Vortex rotation indicated by arrows.

6.2 Streak Length Scales

The mesh on the shroud easily meets classical LES mesh requirements for a channel flow simulation. The average span-wise spacing is $\Delta z^+ = 5.2$, and the average wall-normal spacing is $r^+ = 0.22$. The radial extent of the streaks is quite consistent across the simulations too - their core is at $r^+ \approx 15 - 20$, and they extend out to $r^+ \approx 30 - 40$. However, a significant feature of Fig. 7b is that the shroud heat transfer does not converge as the mesh is refined. This mesh dependency is unexpected given that the near-wall meshes meet the usual requirements.

Investigating the span-wise extent of the streaks in the $r - z$ plane yields some explanation. The distribution of the tangential vorticity, ω_ϕ , from the LES simulation is shown in Fig. 17. The figure shows the cavity in the near shroud region. The region shown in this figure roughly corresponds to $0 < r^+ < 63$.

The vorticity of each streak is concentrated to within 1-3 cells width. This is hardly enough cells to reliably resolve an important flow structure. For mesh convergence, the streaks should be better resolved by, for example, at least 10 cells as suggested by Sagaut [37].

6.3 Modelling Fidelity Effects

The URANS solution in Fig. 16c does not predict the formation of any streaks until close to the end of the cyclonic region - there are weak streaks that raise the local Nu_{sh} to about 7 just before the cyclonic flow separates from the shroud to flow radially inwards. In contrast, the streaks in the LES and DES computations in Fig. 16a and b raise the local Nu_{sh} to about 20 in some regions and start adjacent to where the radial arm meets the shroud.

The question is that, as URANS does not predict streaks, why does it give similar heat transfer to DES and LES? We see that this is because in the URANS solution, the radial arm (positive radial velocity) does not breakdown into smaller structures to the same extent as LES or DES. This means it enhances heat transfer by impinging upon the shroud as a coherent structure. This is visible in the large region of enhanced heat transfer at the top of Fig. 16c. The other simulations capture the breakdown of the radial arm into smaller structures, leading to a more diffuse radial arm, which in turn creates a much less significant heat transfer enhancement from impingement on the shroud. Although URANS gives a similar shroud heat flux to LES, it does so for the wrong reasons.

It is interesting that there are streaks in the DES results in Fig. 16b given that it uses URANS in near-wall regions. This is because in the near-wall region, the URANS layer in the DES returns negligible turbulent viscosity. Hence the URANS layer behaves as a NLES, allowing the streaks to form, and not suppressing them in the same manner as the pure URANS

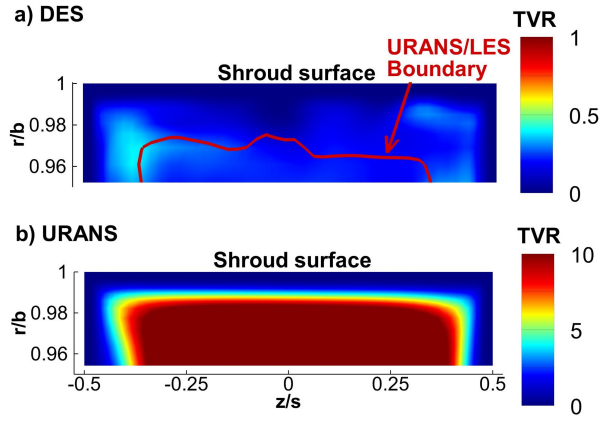


Fig. 18. Near-shroud turbulent viscosity ratio (μ_t/μ) distributions in the cyclonic circulation at the low Grashof number condition.

computations. The reason for this difference in behaviour of URANS and DES (note both use the $k - \omega$ SST model in this region) is the vastly different turbulent viscosities predicted by the models.

Figure 18 shows the near-shroud Turbulent Viscosity Ratio (TVR) in a cyclonic region where streaks have been captured by DES. The TVR is calculated by the ratio of eddy viscosity to the dynamic viscosity, or μ_t/μ . The TVR returned by DES is significantly lower than URANS, even within the URANS region of the URANS/LES hybrid. Note that the scale for DES in Fig. 18a is an order of magnitude smaller than that for URANS in Fig. 18b.

For this particular case, there is no benefit in terms of mesh requirements to using DES over LES, as the flow structures near the wall are captured by the present DES. This does, however, ignore the fact that when not explicitly comparing the models, one would use a much coarser near-wall mesh with DES than LES.

Whilst the DES model in this section performed similarly to LES, its behaviour was inconsistent with being a hybrid URANS/LES model. Whether DES will still behave this way at higher Grashof numbers is unclear and is investigated in the next section.

7 High Grashof Number Simulations

7.1 Modelling Fidelity Effects

The results in the previous section indicate that there may be an issue with the use of DES: both the laminar near-wall layers on the disk (Fig. 10) and the near-shroud streaks (Figs. 16, 18) occur within the RANS region of the DES model. At a low Grashof number this was mitigated by the DES returning a negligible turbulent viscosity near the wall.

To investigate whether this will be the case at higher Grashof numbers, extra simulations were conducted using LES and DES on the same cavity at ten times the rotational speed of the low Grashof number condition, resulting in a Grashof number of 3.03×10^{11} - a 100-fold increase in Gr from the previous condition. The axial Reynolds number was not changed. These simulations had an imposed disk temperature that varied linearly from 330.15 K at the minimum radii of the disk to 378.15 K at the maximum radii of the disk. The shroud temperature was set to be 378.15 K.

The solver set-up was identical to that used for the previous simulations in this paper, expect that the Smagorinsky-Lilly SGS model was used for LES, and the Delayed-DES was used for the URANS/LES hybrid computation [45]. The cavity

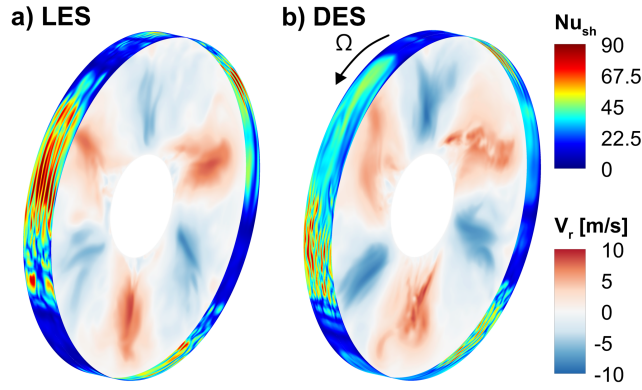


Fig. 19. Shroud Nusselt number and mid-plane radial velocity at the high Grashof number condition.

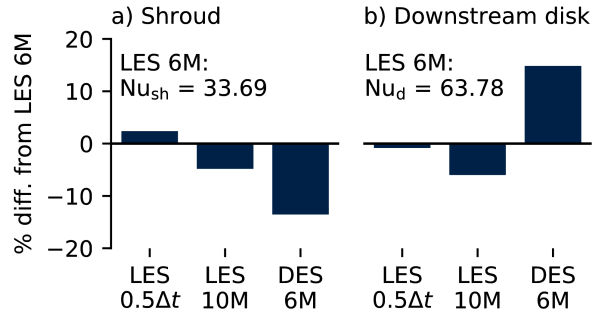


Fig. 20. Comparison of average Nusselt numbers at the high Grashof number condition.

was re-meshed to give an appropriate boundary layer mesh sizing for the new flow condition, resulting in a mesh of 6M cells. 360 time-steps per revolution were used. All solutions were initialised from a coarse mesh laminar solution and ran for 40 revolutions to remove initial transients. Statistics were sampled for 20 revolutions. To confirm the mesh and time-step independence of the conclusions made in this section, the LES computation was repeated on the 6M mesh with 720 steps per revolution and also with a 10M cell mesh again using 360 time-steps per revolution.

As expected, both LES and DES gave the same large-scale flow structure, which consisted of three circulation pairs. This is visible in the radial velocity distributions in Fig. 19.

Despite the large scale similarities in the flow structure, the heat transfer predicted by the two modelling fidelities is quite different - this is shown in Fig. 20. Compared to LES, DES under-predicts the shroud heat transfer by 13.5%, but over-predicts the heat flux through the disk by 14.8%. This inconsistency is still present when compared to LES computations using smaller time steps or a larger number of cells.

Figure 20 helps explain the disparity in the shroud heat transfer calculated by the two modelling fidelities. In the LES (Fig. 20a), there are near-shroud streaks covering a large portion of the cyclonic circulation, causing a heavily enhanced heat transfer in that region. In contrast, the DES (Fig. 20b) has a region of slightly elevated heat transfer early on in the cyclonic circulation, followed by a region of weak streaks towards the end of the circulation. This difference in behaviour is due to the influence of the higher TVR predicted by DES in the near-shroud region (Fig. 21). The RANS branch of the DES in this region is producing enough near-shroud turbulent viscosity to delay the formation of streaks, whilst simultaneously not

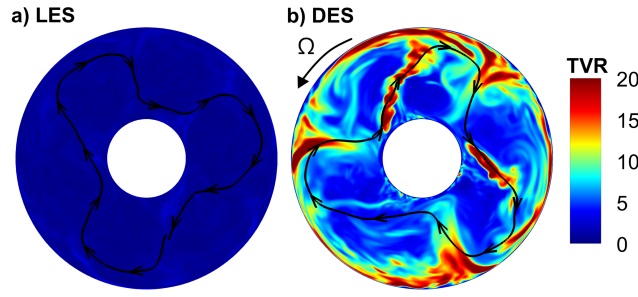


Fig. 21. Mid-plane turbulent viscosity ratio (μ_t/μ) and relative velocity streamlines at the high Grashof number condition.

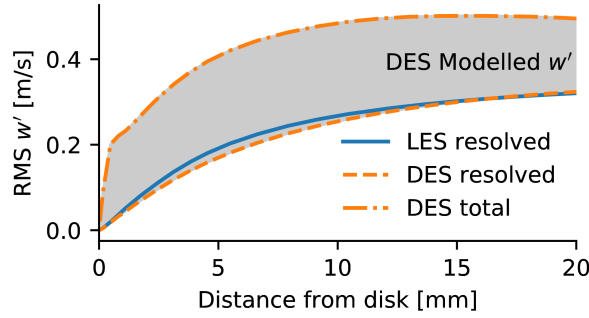


Fig. 22. RMS of wall normal velocity fluctuations (w') near the downstream disk at the mid-radial location.

enhancing the near-shroud heat transfer enough to effectively model the impact of the streaks.

The level of eddy viscosity in Fig. 21a is in line with what one would expect from a LES simulation. The distribution of eddy viscosity in Fig. 21b is indicative of a larger issue with the use of DES for these types of flows. It is clear from this figure that the behaviour of DES is inconsistent with its expected behaviour: the elevated eddy viscosity is not restricted to the near-wall regions, and instead covers the entire domain, where the value of the TVR should be similar to that in Fig. 21a.

The over-prediction of the disk heat transfer can be explained by examining the wall-normal velocity fluctuations near the downstream disk, as shown in Fig. 22. The wall-normal velocity fluctuations are of particular interest as they are responsible for transporting unheated fluid from mid-cavity to the disks. Figure 22 includes the resolved velocity fluctuations from both the LES and the DES, as well as the velocity fluctuations modelled by the DES. It can be seen that DES and LES resolve similar amounts of unsteady transport fluid to and from the wall; however, the DES also models a significant amount of wall-normal velocity fluctuation, creating an unphysical enhancement of the wall heat flux. This double accounting of velocity fluctuations is an issue that is known to affect URANS, so it is not surprising to see it here.

The distribution of the wall-normal LES velocity fluctuation in Fig. 22 is indicative of a laminar near-wall layer. As with Fig 10a for the low Grashof number case, there is no peak, indicating that the near-wall shear is not generating the sort of small-scale unsteady flow layer structures that transport off-wall fluid to and from the wall.

7.2 Further Discussion on DES in Rotating Cavity Flows

DES relies on the existence of a flow-regime gap where the near-wall and bulk fluid have distinct behaviour and are reasonably separate. The near-wall RANS behaviour of DES is made to collapse to LES behaviour in the bulk flow by enhancing

the destruction of eddy viscosity away from the wall. In this flow, the eddy viscosity is injected from the shroud into the bulk flow by radial inflow (shown by the streamlines in Fig. 21b). Thus, the eddy viscosity is advected to a region where it physically should not be. It is worth noting that this non-physical transport of eddy viscosity has also been observed in URANS simulations of HP turbines [14]. The presence of the elevated eddy viscosity in the bulk flow is concerning. It means that the double counting of the unsteady flow is not just restricted to the near-wall layers as shown in Fig. 22, but affects the entire domain.

It is possible that alternative URANS/LES blending functions would reduce this issue by increasing the destruction of the eddy viscosity in LES regions. However, this addresses the symptom rather than the actual problem, so it would be impossible to know *a priori* whether a particular simulation would be free from it. As it stands in the current DES simulation, the "grey area" where both URANS and LES are present covers the whole cavity. Even if, with an appropriate blending function, the URANS domain could be restricted to near-wall regions, the behaviour that a CFD user can expect from the simulation is still unclear. This is due to the presence of important heat transfer enhancing structures (streaks) at a similar wall distance to the URANS/LES switch, as shown in Fig. 18.

Whilst from these results it is clear that caution is needed when employing DES to research rotating cavities, it is also worth noting that these results may also have implications for future developments of wall-modelled LES. As transport equations of some type are necessary to take into account the effects of boundary layer history (precluding a local wall-model), care will need to be taken to ensure that the effects of any new wall-model are restricted to the wall.

8 Conclusions

This paper has presented numerical simulations of a rotating cavity with axial throughflow at Grashof numbers of 3.03×10^9 and 3.03×10^{11} . It has systematically studied the effects of three modelling fidelities (URANS, DES, and LES) and mesh resolution. Simulations were verified in a mesh refinement study, and validated against experimental disk heat transfer data. There are multiple physical mechanisms that dominate in different areas of the flow, these mechanisms are distinct enough for it to be necessary to treat them differently in terms of both mesh resolution and adequate modelling fidelity. The main conclusions from this paper are:

1. Using adiabatic instead of isothermal disks changes the radius at which the radial direction of the near-disk flow reverses, indicating a significant feedback of wall heat transfer to aerodynamics. It is worth investigating CHT simulations to attempt to better capture the aerodynamics of the cavity flow.
2. At the low Grashof number condition, the disk heat transfer was found to be insensitive to the modelling fidelity. The eddy viscosity present in the URANS solution prevented URANS from predicting the formation of coherent shroud streaks accurately. Surprisingly, DES also captured the formation of such streaks, despite being in URANS mode in the near-shroud region. The normalised mesh wall spacings for LES indicated that the streaks were well resolved. In the LES, the vorticity of the streaks was found to be concentrated to within 1-3 cells width. This is very few cells for an important flow structure and indicates that wall mesh spacings alone are not enough to assess LES mesh resolution in

this region.

3. At the high Grashof number condition, the near-shroud streaks were observed to be much weaker in the DES than the LES, reducing the shroud heat transfer. In contrast, on the disks, DES double accounted for the wall-normal velocity fluctuations, causing enhanced heat transfer. In the LES, a near-wall peak in the disk-normal velocity fluctuation was not observed, indicating that the near-disk layer remains laminar even at the high Grashof number condition.
4. DES behaved inconsistently with its expected behaviour in all simulations (in different ways). Locally generated modelled turbulence was observed to be injected from the shroud into the bulk flow by the radial inflow, contaminating the entire solution with an elevated eddy viscosity.

These results contribute to a more consistent understanding of the flow structures in rotating cavities, and what mesh resolution and modelling fidelities are necessary to consistently model them. In particular, the behaviour of DES is a cause for concern. The radial inflow that injected the locally generated modelled turbulence in to the bulk flow is a characteristic feature of rotating cavity flows, and indicates that caution is necessary when simulating rotating cavity flows with wall modelling approaches that do not enforce a strong separation between their modelled and resolved regions.

Acknowledgements

The authors would like to thank the UK Engineering and Physical Science Research Council (EPSRC) for supporting the first author's DPhil. Thanks are also given to the anonymous reviewers, whose comments have helped improve this paper.

Nomenclature

a	[m]	Cavity inner radius
b	[m]	Cavity outer radius
c	[J/kgK]	Specific thermal capacity
D	[m]	Bore hydraulic diameter $= 2(a - r_s)$
f	[Hz]	Frequency
Gr	[-]	Grashof number $= (1 - a/b)^3 Re_\phi^2 \beta \Delta T_{\max}$
k	[W/mK]	Thermal conductivity
Nu_d	[-]	Disk Nusselt number $= qr/k\Delta T_w$
Nu_{sh}	[-]	Shroud Nusselt number $= q(s/2)/k\Delta T_{sh}$

r	[m]	Radial coordinate
r_s	[m]	Shaft radius
Re_z	[-]	Axial Reynolds number $= V_z D / \nu_{in}$
Re_ϕ	[-]	Rotational Reynolds number $= \Omega b^2 / \nu_{in}$
Ro	[-]	Rossby number $= V_z / \Omega a$
s	[m]	Shroud width
T	[K]	Temperature
V_r, V_ϕ, V_z	[m/s]	Radial, relative tangential, and axial velocities
y^+	[-]	Normalised wall spacing
z	[m]	Axial coordinate
α	[m ² /s]	Thermal diffusivity
$\beta \Delta T$	[-]	Buoyancy parameter $= (T - T_{in}) / T_{in}$
δ^*	[m]	Computational Ekman layer thickness
δ_{Ek}	[m]	Theoretical Ekman layer thickness
μ	[Pa s]	Dynamic viscosity
μ_t	[Pa s]	Turbulent eddy viscosity
ν	[m ² /s]	Kinematic viscosity
ρ	[kg/m ³]	Density
τ_{rr}	[Pa]	Radial shear stress
ϕ	[rad]	Tangential coordinate
ω_ϕ	[1/s ²]	Tangential vorticity
Ω	[rad/s]	Rotational speed

Abbreviations

DES	Detached Eddy Simulation
LES	Large Eddy Simulation
NLES	Numerical LES
PSD	Power Spectral Density
SGS	Sub-Grid Scale
TKE	Turbulent Kinetic Energy
TVR	Turbulent Viscosity Ratio
URANS	Unsteady Reynolds Averaged Navier-Stokes

References

- [1] Atkins, N. R., 2013. “Investigation of a Radial-Inflow Bleed as a Potential for Compressor Clearance Control”. In Proc. ASME Turbo Expo. GT2013–95768.
- [2] Chew, J., and Hills, N. J., 2007. “Computational Fluid Dynamics for Turbomachinery Internal Air Systems”. *Philos. Trans. R. Soc. A Math. Phys. Eng. Sci.*, **365**, pp. 2587–2611.
- [3] Owen, J. M., and Long, C. A., 2015. “Review of Buoyancy-Induced Flow in Rotating Cavities”. *J. Turbomach.*, **137**(11), p. 111001.
- [4] He, L., 2011. “Efficient Computational Model for Nonaxisymmetric Flow and Heat Transfer in Rotating Cavity”. *J. Turbomach.*, **133**(2), p. 021018.
- [5] Farthing, P. R., Long, C. A., Owen, J. M., and Pincombe, J. R., 1992. “Rotating Cavity with Axial Throughflow of Cooling Air: Heat Transfer”. *J. Turbomach.*, **114**(1), pp. 229–236.
- [6] Long, C. A., and Tucker, P. G., 1994. “Shroud Heat Transfer Measurements From a Rotating Cavity With an Axial Throughflow of Air”. *J. Turbomach.*, **116**(3), p. 525.
- [7] Long, C. A., 1994. “Disk Heat Transfer in a Rotating Cavity with an Axial Throughflow of Cooling Air”. *Int. J. Heat Fluid Flow*, **15**(4), pp. 307–316.
- [8] Bohn, D. E., Deutsch, G. N., Simon, B., and Burkhardt, C., 2000. “Flow Visualisation in a Rotating Cavity with Axial Throughflow”. In Proc. ASME Turbo Expo. 2000–GT–0280.
- [9] Atkins, N. R., and Kanjirakkad, V., 2014. “Flow in a Rotating Cavity with Axial Throughflow at Engine Representative Conditions”. In Proc. ASME Turbo Expo. GT2014–27174.
- [10] Puttock-Brown, M. R., Rose, M. G., and Long, C. A., 2017. “Experimental and Computational Investigation of Rayleigh-Bénard Flow in the Rotating Cavities of a Core Compressor”. In Proc. ASME Turbo Expo. GT2017–64884.
- [11] Owen, J. M., and Pincombe, J. R., 1980. “Velocity Measurements Inside a Rotating Cylindrical Cavity with a Radial Outflow of Fluid”. *J. Fluid Mech.*, **99**(1), pp. 111–127.
- [12] Bohn, D., Deuker, E., Emunds, R., and Gorzelitz, V., 1995. “Experimental and Theoretical Investigations of Heat Transfer in Closed Gas-Filled Rotating Annuli”. *J. Turbomach.*, **117**(1), pp. 175–183.

- [13] Tyacke, J., Vadlamani, N. R., Trojak, W., Watson, R., Ma, Y., and Tucker, P. G., 2019. “Turbomachinery Simulation Challenges and the Future”. *Prog. Aerosp. Sci.*, **110**, p. 100554.
- [14] Yao, M., and He, L., 2020. “Implicit Discontinuous Galerkin Solution on Unstructured Mesh for Turbine Blade Secondary Flow”. *J. Turbomach.*, **142**(1), p. 011004.
- [15] Long, C. A., and Tucker, P. G., 1994. “Numerical Computation of Laminar Flow in a Heated Rotating Cavity with an Axial Throughflow of Air”. *Int. J. Numer. Methods Heat Fluid Flow*, **4**(4), pp. 347–365.
- [16] Bohn, D., Ren, J., and Tuemmers, C., 2006. “Investigation of the Unstable Flow Structure in a Rotating Cavity”. In Proc. ASME Turbo Expo. GT2006–90494.
- [17] Bohn, D., and Ren, J., 2009. “How Far Have We Been?”. *Front. Energy Power Eng. China*, **3**(4), pp. 489–497.
- [18] Bohn, D., Krewinkel, R., and Wolff, A., 2013. “Numerical Analysis of Heat Transfer and Flow Stability in an Open Rotating Cavity Using the Maximum Entropy Production Principle”. *J. Turbomach.*, **135**(4), p. 041023.
- [19] Tucker, P. G., 2011. “Computation of Unsteady Turbomachinery Flows: Part 2-LES and Hybrids”. *Prog. Aerosp. Sci.*, **47**(7), pp. 546–569.
- [20] Palkin, E., Mullyadzhannov, R., Hadziabdic, M., and Hanjalic, K., 2016. “Scrutinizing URANS in Shedding Flows: The Case of Cylinder in Cross-Flow in the Subcritical Regime”. *Flow, Turbul. Combust.*, **97**(4), pp. 1017–1046.
- [21] Tucker, P. G., 2013. “Trends in Turbomachinery Turbulence Treatments”. *Prog. Aerosp. Sci.*, **63**, pp. 1–32.
- [22] Rubini, R., Maffulli, R., and Arts, T., 2018. “Effect of the Gas to Wall Temperature Ratio on the Bypass Transition”. In Proc. ASME Turbo Expo, pp. GT2018–76214.
- [23] Owen, J. M., Abrahamsson, H., and Lindblad, K., 2007. “Buoyancy-Induced Flow in Open Rotating Cavities”. *J. Eng. Gas Turbines Power*, **129**(4), pp. 893–900.
- [24] Tan, Q., Ren, J., and Jiang, H., 2009. “Prediction of Flow Features in Rotating Cavities with Axial Throughflow by RANS and LES”. In Proc. ASME Turbo Expo. GT2009–59428.
- [25] Tan, Q., Ren, J., and Jiang, H., 2014. “Prediction of 3D Unsteady Flow and Heat Transfer in Rotating Cavity by Discontinuous Galerkin Method and Transition Model”. In Proc. ASME Turbo Expo. GT2014–26584.
- [26] Dweik, Z., Briley, R., Swafford, T., and Hunt, B., 2009. “Computational Study of the Heat Transfer of the Buoyancy-Driven Rotating Cavity with Axial Throughflow of Cooling Air”. In Proc. ASME Turbo Expo. GT2009–59978.
- [27] Sun, Z., Lindblad, K., Chew, J., and Young, C., 2007. “LES and RANS Investigations Into Buoyancy-Affected Convection in a Rotating Cavity With a Central Axial Throughflow”. *J. Eng. Gas Turbines Power*, **129**(2), pp. 318–325.
- [28] Puttock-Brown, M. R., and Rose, M. G., 2018. “Formation And Evolution of Rayleigh-Bénard Streaks in Rotating Cavities”. In Proc. ASME Turbo Expo. GT2018–75497.
- [29] Tateishi, A., Watanabe, T., and Himeno, T., 2018. “Unsteady Flow Simulation of Buoyancy-Driven Flows in High-Pressure Compressor Disk Cavities”. In Proc. ASME Turbo Expo. GT2018–76327.
- [30] Kouwa, J., Iso, Y., Polidoro, F., and Gautier, S., 2018. “Very-Large Eddy Simulations of Disk Heat Transfer in a Rotating Cavity Using Lattice-Boltzmann Method”. In Proc. ASME Turbo Expo, Vol. 5B-2018, ASME. GT2018–76832.

- [31] He, L., and Yi, J., 2017. “Two-Scale Methodology for URANS/Large Eddy Simulation Solutions of Unsteady Turbomachinery Flows”. *J. Turbomach.*, **139**(10), p. 101012.
- [32] Pitz, D. B., Chew, J. W., and Marxen, O., 2019. “Effect of an Axial Throughflow on Buoyancy-Induced Flow in a Rotating Cavity”. *Int. J. Heat Fluid Flow*, **80**.
- [33] Pitz, D. B., Chew, J., and Marxen, O., 2019. “Large-Eddy Simulation of Buoyancy-Induced Flow in a Sealed Rotating Cavity”. *J. Eng. Gas Turbines Power*, **141**(2), p. 021020.
- [34] Sun, Z., Amirante, D., Chew, J., and Hills, N. J., 2015. “Coupled Aerothermal Modeling of a Rotating Cavity With Radial Inflow”. *J. Eng. Gas Turbines Power*, **138**(3), p. 032505.
- [35] Onori, M., Amirante, D., Hills, N. J., and Chew, J. W., 2016. “LES Validation for a Rotating Cylindrical Cavity with Radial Inflow”. In Proc. ASME Turbo Expo. GT2016–56393.
- [36] Onori, M., Amirante, D., Hills, N. J., and Chew, J. W., 2019. “Heat Transfer Prediction From Large Eddy Simulation of a Rotating Cavity With Radial Inflow”. *J. Eng. Gas Turbines Power*, **141**(12), p. 121002.
- [37] Sagaut, P., 2006. *Large Eddy Simulation for Incompressible Flows*. Springer-Verlag.
- [38] Menter, F., 1994. “Two-Equation Eddy-Viscosity Turbulence Models for Engineering Applications”. *AIAA J.*, **32**(8), pp. 1598–1605.
- [39] Nicoud, F., and Ducros, F., 1999. “Subgrid-Scale Stress Modelling Based on the Square of the Velocity Gradient Tensor”. *Flow, Turbul. Combust.*, **62**(3), pp. 183–200.
- [40] Menter, F., 2018. “Stress-Blended Eddy Simulation (SBES) — A New Paradigm In Hybrid RANS-LES Modeling”. *Notes Numer. Fluid Mech. Multidiscip. Des.*, **137**, pp. 27–37.
- [41] Tian, S., and Zhu, Y., 2012. “Disk Heat Transfer Analysis in a Heated Rotating Cavity with an Axial Throughflow”. In Proc. ASME Turbo Expo. GT2012–69185.
- [42] Childs, P. R. N., 2011. *Rotating Flow: Fundamentals*. Elsevier.
- [43] He, L., 2019. “Closely Coupled Fluid-Solid Interface Method with Moving-Average for LES Based Conjugate Heat Transfer Solution”. *Int. J. Heat Fluid Flow*, **79**, p. 108440.
- [44] Faghri, A., Zhang, Y., and Howell, J. R., 2010. *Advanced Heat and Mass Transfer*. Global Digital Press.
- [45] Gritskevich, M. S., Garbaruk, A. V., Schütze, J., and Menter, F. R., 2012. “Development of DDES and IDDES Formulations for the k- ω Shear Stress Transport Model”. *Flow, Turbulence and Combustion*, **88**, 4, pp. 431–449.